Simulations of X-ray diffraction of shock-compressed single-crystal tantalum with synchrotron undulator sources

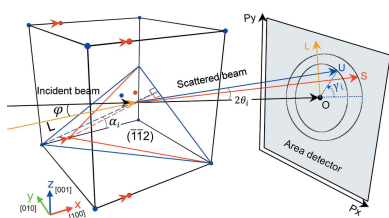## M. X. Tang,[a] Y. Y. Zhang,[a] J. C. E[a] and S. N. Luo[a,b]*

[a]The Peac Institute of Multiscale Sciences, Chengdu, Sichuan 610031, People's Republic of China, and [b]Key Laboratory of Advanced Technologies of Materials, Ministry of Education, Southwest Jiaotong University, Chengdu, Sichuan 610031, People's Republic of China. *Correspondence e-mail: sluo@pims.ac.cn

Polychromatic synchrotron undulator X-ray sources are useful for ultrafast single-crystal diffraction under shock compression. Here, simulations of X-ray diffraction of shock-compressed single-crystal tantalum with realistic undulator sources are reported, based on large-scale molecular dynamics simulations. Purely elastic deformation, elastic–plastic two-wave structure, and severe plastic deformation under different impact velocities are explored, as well as an edge release case. Transmission-mode diffraction simulations consider crystallographic orientation, loading direction, incident beam direction, X-ray spectrum bandwidth and realistic detector size. Diffraction patterns and reciprocal space nodes are obtained from atomic configurations for different loading (elastic and plastic) and detection conditions, and interpretation of the diffraction patterns is discussed.

1. Introduction

Dynamic materials response is multiscale in nature, from bulk scale stress–strain curves to mesoscale strain fields and down to microscale lattice deformation, and real time measurements of such quantities are crucial (Lu *et al.*, 2016, 2017*a*,*b*). At the crystal lattice scale, X-ray diffraction measurements are a key means to probe a shock-compressed solid. Because of the short duration of shock events, typically sub-millisecond to nanoseconds, high-brilliance high-coherence X-ray sources such as synchrotron undulator sources and X-ray free-electron laser (XFEL) facilities have become increasingly important for transient X-ray diffraction measurements under Hopkinson bar, gas gun and laser loading (Lu *et al.*, 2016; Huang *et al.*, 2016; Luo *et al.*, 2012; Fan *et al.*, 2016; Gupta *et al.*, 2012; Ichiyanagi *et al.*, 2007; Ichiyanagi & Nakamura, 2016; DeCamp *et al.*, 2005; Thierry d'Almeida *et al.*, 2002; Turneaure *et al.*, 2017; Wehrenberg *et al.*, 2017).

Ultrafast diffraction measurements on single crystals suffer from the narrow bandwidth of undulator sources and the small size of fast detectors, for both synchrotron and XFEL experiments (Fan *et al.*, 2016; Liss *et al.*, 2009; Gupta *et al.*, 2012; DeCamp *et al.*, 2005; Thierry d'Almeida *et al.*, 2002; Wehrenberg *et al.*, 2017; Kraus *et al.*, 2016). Previous single-shot XFEL measurements mostly reported diffraction from polycrystalline solids (Wehrenberg *et al.*, 2017; Kraus *et al.*, 2016). It is not uncommon that only one or two diffraction spots are captured at a given instant when it comes to single-crystal diffraction. For shock compression, an interesting question is the relation between lattice strain obtained from diffraction patterns and macroscopic or bulk strain, in addition

to crystal structure determination. Obtaining such information from one or two diffraction spots is indeed a challenging issue; systematic forwarding modeling/simulation is highly desirable as a complement to dynamic diffraction measurements, but still rare.

In order to guide experimental design and help data interpretation, we have performed large-scale molecular dynamics (MD) simulations and X-ray diffraction of shock-compressed single-crystal tantalum with realistic undulator sources at the Advanced Photon Source, USA. We systematically explore different loading conditions, including purely elastic deformation, elastic–plastic two-wave structure, and severe plastic deformation under different impact velocities, as well as an edge release case, for diffraction simulations based on atomic configurations. Transmission-mode diffraction simulations consider crystallographic orientation, loading direction, incident beam direction, X-ray spectrum bandwidth and realistic detector size. Diffraction patterns and reciprocal space nodes are obtained from atomic configurations for different loading and detection conditions, and interpretation of the diffraction patterns is discussed. In particular, for a one-dimensional strain condition, lattice strain along the shock direction is obtained from a single Laue spot before and after shock compression based on the Laue diffraction geometry, and this lattice strain can represent bulk strain for pure elastic deformation; upon plastic deformation, lattice deformation changes from one- to three-dimensional compression (Bringa *et al.*, 2006; Rigg & Gupta, 2001) and the deviation of lattice strain from bulk strain increases with increasing plastic deformation.

2. Methodology

For MD simulations of shock compression of tantalum single crystals, the Large-scale Atomic/Molecular Massively Parallel Simulator (Plimpton, 1995) and an embedded-atom method (EAM) potential (Ravelo *et al.*, 2013) are used. This EAM potential is accurate for describing the properties of tantalum as shown by numerous shock and nonshock simulations (Wang *et al.*, 2014; Hahn *et al.*, 2017; Lane *et al.*, 2016; Tang *et al.*, 2017).

We construct an idealized tantalum single crystal with dimensions of about 119 nm × 83 nm × 83 nm, corresponding to 45 million atoms. Prior to shock loading, the configuration is relaxed at 0 K, and then annealed with the constant-pressure–temperature ensemble under three-dimensional periodic boundary conditions at 300 K and zero pressure. Shock compression simulations are performed with the microcanonical ensemble (Wang *et al.*, 2014, 2015). The shock loading direction is along [100] (the *x*-axis); the *y*- and *z*-axes are along [010] and [001], respectively. For shock simulations, a free-surface boundary is applied along the *x*-axis; periodic boundary conditions are or are not applied along the *y*- and *z*-axes for simulations without or with edge release, respectively. The time step for integration of the equation of motion is 1 fs. A small region on the left-hand side of a sample is set as the piston to drive the shock (Holian, 1995). The interactions between the piston and the rest of the atoms in the config-

uration are described with the same interatomic potential, while the atoms in the piston do not participate in molecular dynamics in the impact simulations without edge release. Physical quantities such as particle velocity, density, stress and temperature can be obtained from trajectories *via* binning analysis (Luo *et al.*, 2009), and the corrections for the velocity of the center of mass of each bin are considered.

Atomic configurations from MD shock simulations are used as input to diffraction-related calculations, which are conducted with *GAPD*, a GPU-accelerated atom-based polychromatic diffraction simulation code (E *et al.*, 2018). *GAPD* can compute reciprocal space nodes and X-ray diffraction patterns for an arbitrary geometry and polychromatic X-rays as from a 'white-beam' undulator source. The scattered intensity $I(\mathbf{q})$ is

$$I(\mathbf{q}) = \frac{F(\mathbf{q})\,F^*(\mathbf{q})}{N}, \quad (1)$$

with the structure factor

$$F(\mathbf{q}) = \sum_{j=1}^{N} f_j \exp\left(2\pi i \mathbf{q} \cdot \mathbf{r}_j\right). \quad (2)$$

Here, $\mathbf{q}$ is the reciprocal space vector or scattering vector, $\mathbf{r}$ is the position of an atom in the real space, f is the atomic scattering factor for electrons or X-rays (Prince, 2004), and N is the number of atoms in the selected area or volume. For a given wavelength λ, the diffraction angle 2θ and $\mathbf{q}$ are related *via* Bragg's law (Warren, 1969; Williams & Carter, 2009),

$$\frac{2\sin\theta}{\lambda} = \frac{1}{d_{hkl}} = |\mathbf{q}|, \quad (3)$$

where d represents the spacing between neighboring (hkl) planes, *i.e.* the *d*-spacing.

The Lorentz-polarization factor (Warren, 1969) for X-ray diffraction,

$$\mathrm{Lp}(\theta) = \frac{1 + \cos^2 2\theta}{\cos\theta\sin^2\theta}, \quad (4)$$

is considered here. Then the X-ray diffraction intensity $I_x(\mathbf{q})$ follows as

$$I_x(\mathbf{q}) = \mathrm{Lp}(\theta)\,\frac{F(\mathbf{q})\,F^*(\mathbf{q})}{N}. \quad (5)$$

For a polychromatic beam, the intensity at a specific position on a two-dimensional detector, $I_{\mathrm{poly}}(2\theta, \gamma)$, is the weighted integration over the incident beam wavelength range, $[\lambda_a, \lambda_b]$,

$$I_{\mathrm{poly}}(2\theta, \gamma) = \frac{\int_{\lambda_a}^{\lambda_b} I(2\theta, \gamma, \lambda)\,w(\lambda)\,\mathrm{d}\lambda}{\int_{\lambda_a}^{\lambda_b} w(\lambda)\,\mathrm{d}\lambda}. \quad (6)$$

Here, γ denotes the azimuthal angle of the diffraction patterns (Fig. 1), and $w(\lambda)$ is the flux of the incident beam spectrum. Each set of $(2\theta, \gamma, \lambda)$ corresponds to a scattering vector $\mathbf{q}$. Details on intensity calculation and intensity projection onto a detector have been presented elsewhere (E *et al.*, 2018).
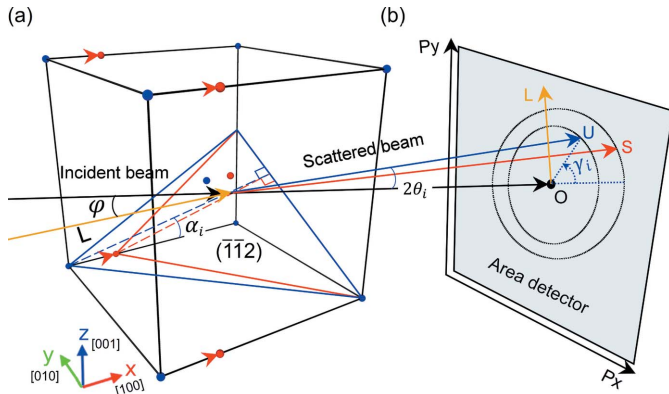
Figure 1
(*a*) Typical transmission geometry for X-ray diffraction of a tantalum single crystal under shock loading. The crystal and sample coordinate systems coincide here. φ is the acute angle between the incident beam and loading direction (L); α_i (i = 1, 2) denote the angles between the loading direction and diffraction planes ($\bar{1}\bar{1}2$), colored in blue and red for unshocked (U) or shocked (S) portions, respectively. (*b*) Projection screen or area detector. O is the origin of the detector coordinate system, the intersection of the incident beam with the screen. OL is the projection of the compression direction. Angles γ_i (i = 1, 2, L) denote the azimuthal angles of the diffraction patterns or OL.

The diffraction geometry for a tantalum single crystal under shock compression (uniaxial strain condition) is shown in Fig. 1. The crystal coordinate system coincides with the sample coordinate system. The incident beam direction is arbitrary but remains perpendicular to the projection screen or area detector, and they intersect at O on the screen. The sample–detector distance is fixed at 250 mm, and increasing/decreasing this distance will increase/decrease the spacing between diffraction spots on the detector. O is the origin of the detector coordinate system $P_x P_y$.

Upon elastic, uniaxial strain, compression along [100], the lattice is compressed along the *x*-axis (Fig. 1*a*), leading to deformation of some lattice planes. In the transmission-mode diffraction, the *d*-spacing method, which uses Bragg's law to calculate *d*-spacings and then lattice strains, is not suitable for calculating the lattice strain along the compression direction in this case. Instead, we calculate the strain on the basis of Laue diffraction geometry. For instance, the ($\bar{1}\bar{1}2$) plane deforms from the blue triangle for the unshocked state to the red triangle for the shocked state. The acute angle between the incident beam and the compression direction is φ, and the corresponding diffraction angles are $2\theta_1$ and $2\theta_2$ and azimuthal angles are γ_1 and γ_2 for the unshocked (U; subscript 1) and shocked (S; subscript 2) states, respectively. The angles between the loading direction and the diffraction planes, α_i (i = 1, 2), for the unshocked and shocked states, respectively, follow as

$$\alpha_i = \left| \frac{\pi}{2} - \arccos\left[-\sin\theta_i \cos\varphi + \sin\varphi \cos\theta_i \cos(\gamma_i - \gamma_L) \right] \right|. \tag{7}$$

Here, γ_L is the azimuthal angle of the compression direction projected on the area detector (Fig. 1*b*). α_1 and α_2 can be used
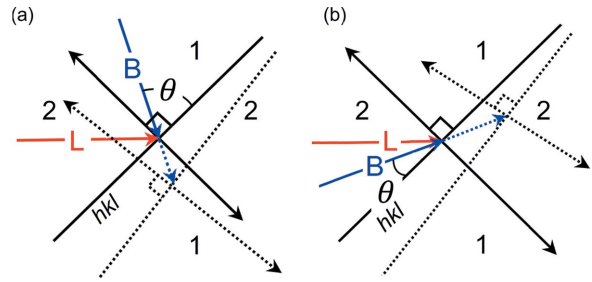

Figure 2
(*a*, *b*) Half diffraction angle on the plane defined by the incident beam direction (B), the loading direction (L), and the normal of diffracting planes, (hkl). The view direction is parallel to the (hkl) planes. Solid lines and dotted lines denote the unshocked and shocked configurations, respectively.

to calculate the elastic uniaxial lattice strain along the compression direction (ε_1) for the transmission geometry as

$$\varepsilon_1 = 1 - \frac{\tan\alpha_2}{\tan\alpha_1}. \tag{8}$$

Depending on diffraction geometry, diffraction angle may increase or decrease upon shock compression. As shown in Fig. 2(*a*), an (hkl) plane and its plane normal form quadrants (*e.g.* 1 and 2). When the loading direction and incident beam direction belong to different quadrants (*e.g.* 1 and 2, respectively), the diffraction angle decreases upon compression. On the other hand, when the loading direction and the incident beam direction belong to the same quadrant (*e.g.* 2), the diffraction angle increases upon compression (Fig. 2*b*).

In order to provide guidance for synchrotron experiments, we use *XOP* (Sánchez del Río & Dejus, 2004) to simulate typical X-ray spectra used in experiments at beamline 32-ID of the Advanced Photon Source (APS) (Fig. 3). We use two undulator X-ray sources in the 'white beam' mode. The undulators consist of dipole magnets with periods of 18 mm
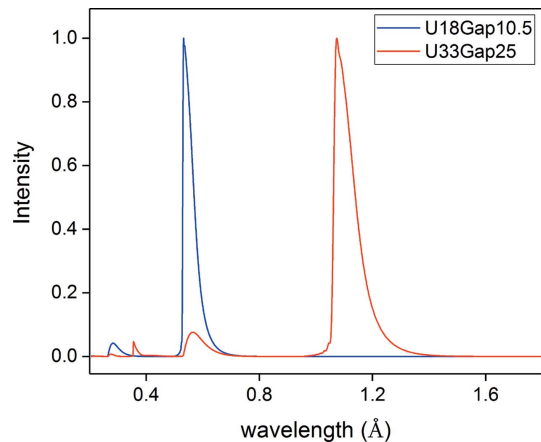

Figure 3
Simulated X-ray spectra from two typical APS undulator sources, through a 1 mm × 1 mm pinhole located at 35 m away from the source. U18Gap10.5: undulator with a period of 18 mm and a gap of 10.5 mm; U33Gap25: undulator with a period of 33 mm and a gap of 10.5 mm. The electron energy is 7 GeV and the current is 100 mA. The spectral flux is normalized by the peak value.

(U18) and 32 mm (U32), and are operated at a gap of 10.5 mm and 25 mm, respectively. These spectra will be used to calculate X-ray diffraction patterns based on the atomic configurations from MD simulations.

3. Results and discussion

3.1. Shock loading

For MD simulations, we explore four shock compression cases at different piston velocities (u_p), without and with edge release (Fig. 4). The shock direction is along [100] (the x-axis) for all of the cases. For $u_p = 0.2$ km s^{-1}, single-crystal tantalum undergoes purely elastic deformation, corresponding to a shock stress of $\sim$15 GPa. A stable elastic shock is observed for the case without edge release (Fig. 4a), while the leading part of the elastic shock wave is attenuated due to edge release when free surfaces are present along the y- and z-axes (Fig. 4b). Above the Hugoniot elastic limit, the elastic–plastic two-wave structure appears for $u_p = 0.75$ km s^{-1} (Fig. 4c), and the peak shock stress is about 56 GPa. For a much stronger shock ($u_p = 2$ km s^{-1}, peak stress = 195 GPa; Fig. 4d), the elastic wave is overtaken by the plastic wave and only a single wave (plastic) is observed (Ravelo *et al.*, 2013). We examine below X-ray diffraction of the target under shock loading for the above four representative cases, and associated structure, lattice strain and bulk strain.

3.2. Displacement of reciprocal space nodes induced by elastic shock compression

The single-crystal tantalum is subjected to shock compression along [100] (the x-axis) at a piston velocity of 0.2 km s^{-1}, and undergoes purely elastic deformation. We calculate representative reciprocal space nodes of the partially compressed configuration, along with Ewald spheres for polychromatic X-rays (Fig. 5). The Ewald sphere representation (Fig. 5a) can supply useful guidance to how to design a diffraction geometry and choose an appropriate X-ray spectrum, ensuring that an Ewald sphere intercepts a node under consideration at the **q** point with the maximum intensity to produce diffraction signals on the area detector.

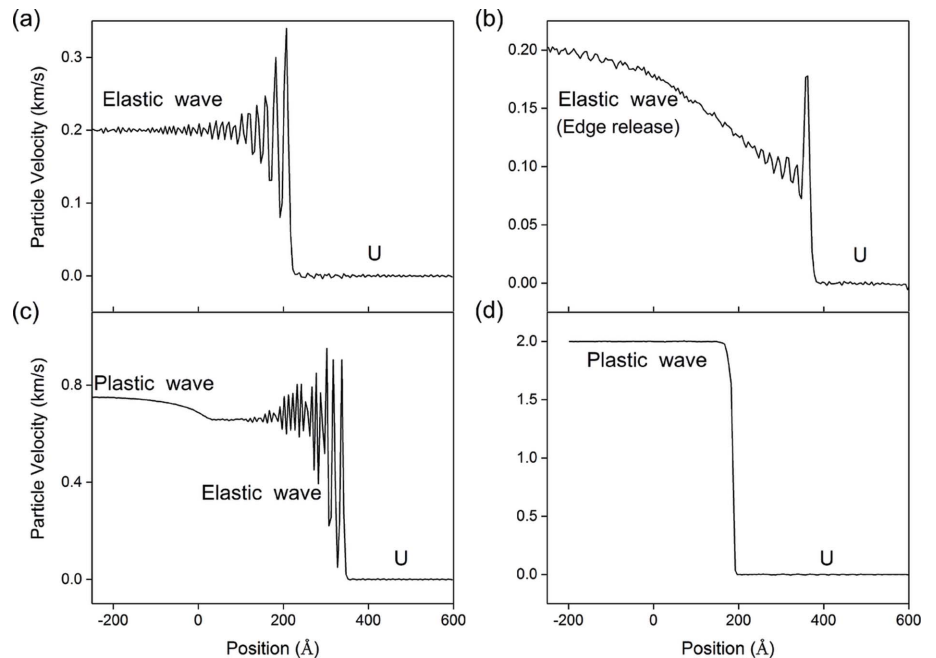For uniaxial strain (compression) along [100], different reciprocal space

Figure 4
One-dimensional velocity profiles of tantalum under shock compression. (a) $u_p = 0.2$ km s^{-1} without edge release at $t = 15$ ps. (b) $u_p = 0.2$ km s^{-1} with edge release at $t = 15$ ps. (c) $u_p = 0.75$ km s^{-1} without edge release at $t = 15$ ps. (d) $u_p = 2$ km s^{-1} without edge release at $t = 10$ ps. U: unshocked.

nodes may behave differently. Fig. 5(b) shows three representative nodes, ($\bar{1}\bar{1}2$), (200) and (020), after the elastic shock propagates into the middle of the target (partial compression). Different from the other two nodes, the (020) node does not move after shock compression, because the lattice compression in this direction is essentially zero. As for the (200) node, the nodes due to the unshocked and shocked portions are well separated (Fig. 5b). The lattice strain along the shock compression direction (one-dimensional strain) can be obtained from the node displacement,

$$\varepsilon_l = \frac{(\mathbf{k}_s - \mathbf{k}_u) \cdot \mathbf{n}_k}{\mathbf{k}_u \cdot \mathbf{n}_k}, \qquad (9)$$
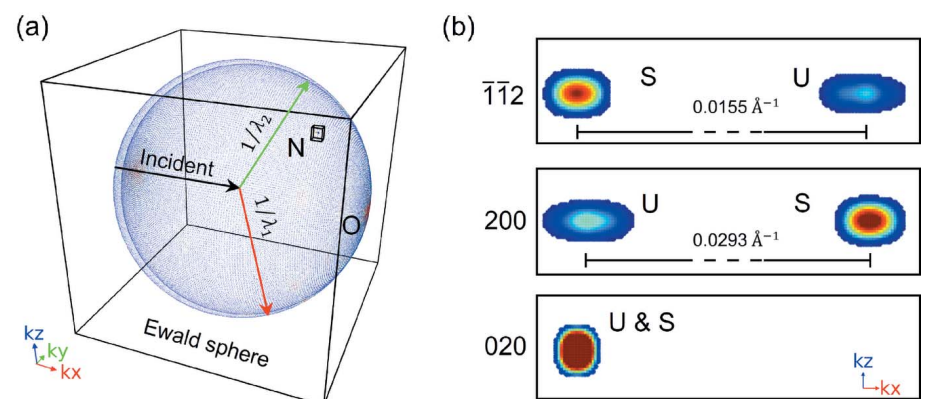

Figure 5
(a) Ewald sphere representation of diffraction with polychromatic X-rays. N denotes reciprocal space nodes, which are intercepted by the Ewald spheres of two representative wavelengths (λ_1^{-1} and λ_2^{-1}). O is the origin of the reciprocal space. (b) Representative reciprocal space nodes during shock compression at 15 ps. U: unshocked; S: shocked; piston velocity: 0.2 km s^{-1}; no edge release.

where k_u and k_s denote the reciprocal space vectors of the nodes corresponding to unshocked and shocked states, respectively. n_k is the unit reciprocal space vector along the compression direction. The displacement from the node center for the unshocked state, (0.6046 Å⁻¹, 0, 0), to the node center for the shocked state, (0.6353 Å⁻¹, 0, 0), corresponds to a lattice strain of 0.04832 along [100] (the shock compression direction).

For the ($\bar{1}\bar{1}2$) node, the node displacement from the unshocked node center (-0.3022 Å⁻¹, -0.3025 Å⁻¹, 0.605 Å⁻¹) to the shocked node center (-0.3177 Å⁻¹, -0.3025 Å⁻¹, 0.605 Å⁻¹), yields a lattice strain of 0.04879. The bulk strain directly calculated from MD simulations is 0.04883, which is in agreement with the lattice strains along the compression direction calculated from the (200) and ($\bar{1}\bar{1}2$) nodes. Thus, the lattice strain in the compression direction obtained from appropriate nodes can represent bulk strain under elastic compression.

3.3. Diffraction patterns for different geometries during elastic shock compression

For single-crystal X-ray diffraction measurements during shock compression, it is difficult to obtain the diffraction spots for unshocked and shocked regions simultaneously, using an undulator source as in Fig. 5, for two reasons: the limited bandwidth (compared with white beam Laue diffraction) and the small detector size (small q-space coverage). In the following discussion, we use U-spot and S-spot to denote the diffraction spots from an unshocked region and a shocked region, respectively. Scattered X-rays come predominantly from the fundamental rather than much weaker high harmonics, but the bandwidth of a fundamental is narrow (e.g. 1–7%). Such measurements require specific diffraction geometry, and adjustment of the undulator gap to yield an appropriate spectrum in order to satisfy Bragg's law. Interpretation of diffraction spots is closely related to the geometry.

A simple geometry is one in which the incident beam direction coincides with the compression direction, i.e. $\varphi = 0$ and $\alpha_i = \theta_i$. This simple geometry requires an appropriate X-ray spectrum, and obtaining appropriate wavelengths in the first harmonic dictates the choice of undulator. For 5% uniaxial lattice strain in the compression direction (the x-axis, [100]), the calculated wavelength is 1.1013 Å for the U-spot ($\bar{1}\bar{1}2$) and 1.1388 Å for the S-spot. Thus, undulator source U33Gap25 is more appropriate (Fig. 3). The X-ray diffraction patterns and corresponding γ–2θ maps are calculated with this X-ray spectrum, and some snapshots are shown in Fig. 6.

Prior to shock compression, the diffraction spot appears at $2\theta = 48.17°$ and $\gamma = 63.44°$. At 12 ps, half of the sample is under elastic compression, leading to the appearance of a new diffraction spot (S). The distance between two diffraction spots is about 10 mm and 20 mm on the projection screen along the P_x and P_y directions, respectively. These distances should be considered for a proper choice of detector and magnification. The diffraction angles for the unshocked and shocked portions of the target are $2\theta = 48.15°$ (U) and $50.29°$ (S), and γ remains unchanged. The diffraction spot U at 12 ps is slightly different from the spot at 0 ps: it is broadened and slightly shifted, as a result of decreased/increased scattering contribution from the unshocked/shocked region. The corresponding lattice strain obtained from equation (7) is about 0.04814, in agreement with $\varepsilon_1 = 0.04879$ calculated from the displacement of the reciprocal space node ($\bar{1}\bar{1}2$). As the shock wave continues to propagate, the unshocked portion becomes smaller, and peak broadening of the unshocked spot (U) becomes more pronounced (18 ps); the U and S spots move slightly to higher angles ($2\theta = 48.26°$ and $50.34°$, respectively), due to the increased/decreased scattering from the shocked/unshocked region. Relative to the spot at 0 ps, the lattice
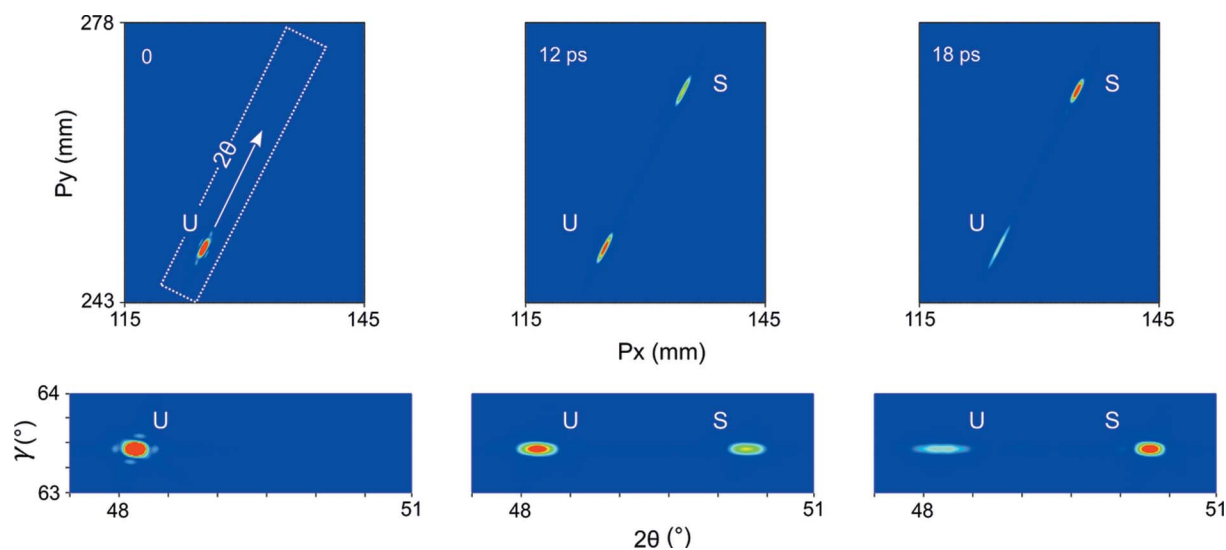

Figure 6
Snapshots of diffraction patterns (top row) for the ($\bar{1}\bar{1}2$) reflection, and the γ–2θ maps (bottom row) corresponding to the area delimited by the dotted rectangle in in the diffraction pattern. Color coding is based on scattering intensity. Shock direction: [100]; incident beam direction: [100]; piston velocity: 0.2 km s⁻¹; no edge release.

strain at 18 ps is 0.04877, closer to the bulk strain of 0.04883. During shock compression, there is a negligible grain rotation (γ remains unchanged).

For different diffraction spots, the lattice strains of corresponding diffraction planes are normally different under one-dimensional strain compression. However, their components along the compression direction can be similar as shown with the reciprocal space nodes in Fig. 5. Given appropriate diffraction spots, the lattice strain along the compression direction, as calculated with equation (7), should also be the same for different reflections. We calculate the diffraction spots for the high-angle ($\bar{2}\bar{2}2$) reflection (Fig. 7) using the same geometry as for the ($\bar{1}\bar{1}2$) reflection (Fig. 6). Similarly, the lattice strain from the U-spot and S-spot at 12 ps is obtained as about 0.04804 along the compression direction, which is close to that using the ($\bar{1}\bar{1}2$) reflection (0.04877) and the bulk strain (0.04883). At 18 ps, the U-spot/S-spot becomes weaker/brighter due to decreased/increased scattering from the unshocked/shocked area while similar strains can be obtained.

Traditionally, a diffraction angle is used to calculate d-spacing based on Bragg's law in the back reflection or Bragg geometry (Kalantar *et al.*, 2003; Gupta *et al.*, 2012), and then lattice strain. Under transmission or Laue geometry, 2θ changes from 48.15° (U) to 50.29° (S) for the ($\bar{1}\bar{1}2$) spots, and the wavelengths obtained from the Ewald spheres are about 1.1013 Å and 1.1373 Å, respectively; the corresponding d-spacings are ~1.34986 Å and 1.33828 Å, and the lattice strain is 0.00858. For the ($\bar{2}\bar{2}2$) spots, 2θ changes from 70.51° (U) to 73.19° (S), and the relevant wavelengths are approximately 1.1019 Å and 1.1189 Å, so the d-spacing is 0.954495 Å and 0.938431 Å, respectively, and the corresponding lattice strain is 0.00163. The lattice strains derived from d-spacings for ($\bar{1}\bar{1}2$) and ($\bar{2}\bar{2}2$) reflections are different, and cannot represent the bulk strain (0.0488) in the transmission geometry.

One should optimize diffraction geometry on the basis of available spectra and possible compression ratios. For tantalum, harder X-rays from U18Gap10.5 are preferred for better penetration. Spectral photon flux and spectrum asymmetry need to be considered to maximize signal intensity, and wavelengths of the probe X-rays between 0.53 Å and 0.57 Å are appropriate. The detector size should also be considered regarding the distance between the U-spot and S-spots, and changes in 2θ and γ.

Given the considerations above, we orient the X-ray incident beam along [$1\bar{1}\bar{1}$] for the [100] compression, to detect the ($\bar{1}\bar{2}3$) reflection. The distances between unshocked and shocked spots are about 4.9 mm and 3.0 mm along the P_x and P_y directions, respectively (12 ps, Fig. 8). As the shocked portion increases, the S-spot becomes brighter while the U-spot becomes dimmer. In this geometry, $\varphi = 54.7356°$, $\gamma_L = 150°$, and the X-ray wavelengths for the unshocked and shocked patterns are about 0.545 Å and 0.555 Å, respectively; 2θ changes from 35.94° to 36.75°, while γ changes from 53.42° to 52.76°, for the U and S spots, respectively (12 ps). The corresponding lattice strain ε_1 is 0.0483 along the shock compression direction, and its error relative to the bulk strain is ~1%.

3.4. Edge release effect during elastic compression

In some experiments, it is of more convenience for the incident X-ray beam to be perpendicular to the shock compression direction. However, an issue is the edge release effect which may complicate diffraction measurements and interpretation. We examine below two identical cases except that one is without and the other is with edge release.

The incident X-ray beam direction is [$0\bar{1}0$], perpendicular to the compression direction, [100]. During shock compression at 12 ps, 2θ for the ($\bar{1}12$) reflection decreases from 48.18° to 47.76°, the λ values for the unshocked and shocked patterns are about 1.1021 Å and 1.0835 Å, respectively, and γ changes from 63.44° to 62.3° (Fig. 9a, without edge release); the
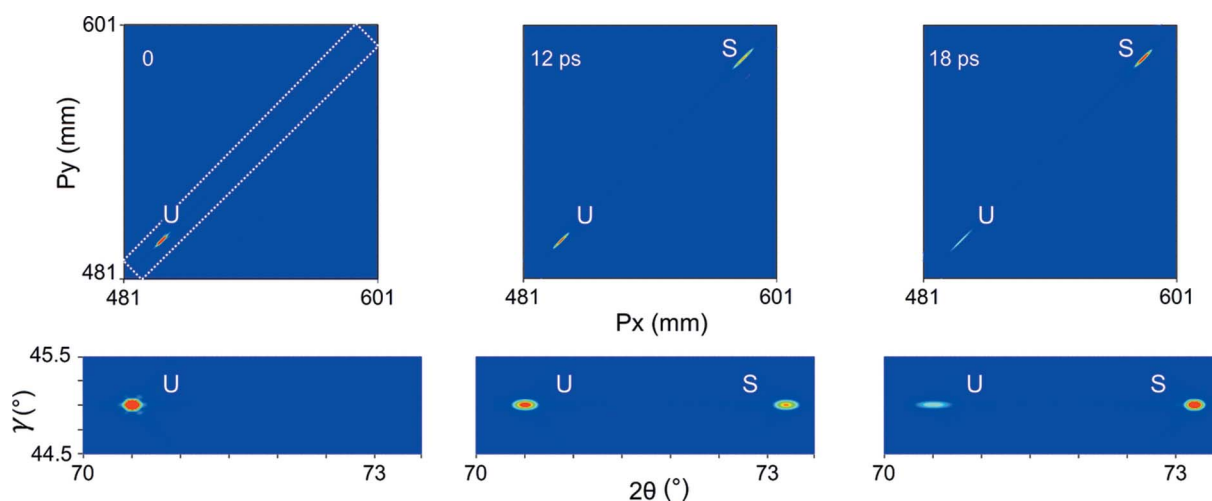

Figure 7
Snapshots of diffraction patterns (top row) for the ($\bar{2}\bar{2}2$) reflection, and the γ–2θ maps (bottom row) corresponding to the area delimited by the dotted rectangle in the diffraction pattern. Color coding is based on scattering intensity. Shock direction: [100]; incident beam direction: [100]; piston velocity: 0.2 km s^{-1}; no edge release.
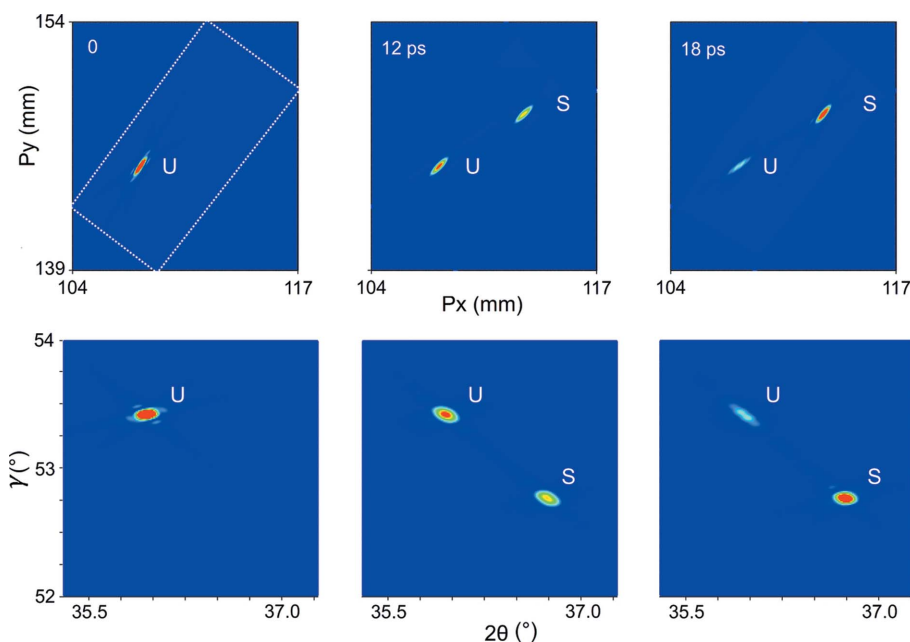
research papers

Figure 8
Snapshots of diffraction patterns (top row) for the ($\bar{1}2\bar{3}$) reflection, and the γ–2θ maps (bottom row) corresponding to the area delimited by the dotted rectangle in the diffraction pattern. Color coding is based on scattering intensity. Shock direction: [100]; incident beam direction: [1$\bar{1}\bar{1}$]; piston velocity: 0.2 km s^{-1}; no edge release.

corresponding strain is $\varepsilon_l = 0.0482$ (within 1% of the bulk strain). The 'abnormal' decrease in 2θ is attributed to the relative orientation between loading direction and incident beam direction, as explained in Fig. 2. In the case of edge release (Fig. 9b), the U-spot is elongated with satellite spots. The S-spot becomes diffuse, broadens along the γ direction, and shifts relative to its counterpart in the case without edge release; its intensity is ten times weaker than the case without edge release. Other weak spots also appear due to nonuniform deformation or more complex elastic strain, and it is difficult to distinguish them from the S-spot. Detection in experiments should consider this intensity reduction, and interpretation becomes complicated as well. Thus, this geometry (shock direction being perpendicular to beam direction) is less favorable in experiments.

3.5. Plastic deformation

Above the Hugoniot elastic limit at $u_p = 0.75$ km s^{-1}, tantalum deforms plastically but retains high crystalline order, and twinning plays a key role (Fig. 10a). However, apparent disordering occurs at 2 km s^{-1} due to catastrophic nucleation of dislocations/twins (Fig. 10b), along with premelting (Ravelo *et al.*, 2013), similar to single-

crystal copper (An *et al.*, 2008). Consequently, the diffraction pattern shows a well defined S-spot for $u_p = 0.75$ km s^{-1}, but a diffuse scattering ring for 2 km s^{-1}. The {112} diffraction spots are from the unshocked portion in the latter case.

For $u_p = 0.75$ km s^{-1}, the S-spot becomes weaker and moves farther along the 2θ direction, and the distances between the U- and S-spots are about 34.5 mm and 69 mm along the P_x and P_y directions, respectively. The λ values for the unshocked and shocked patterns are about 1.102 Å and 1.213 Å, respectively; 2θ changes from 48.17° to 55.14° (Fig. 10c), corresponding to 0.144 lattice strain if we use equation (7); this lattice strain is about 11% lower than the bulk strain (0.162) directly obtained from MD configurations. In plastic deformation, lattice deformation is not one-dimensional, since dislocation slip and deformation twinning induce deformation along other directions different from the loading direction (Bringa *et al.*, 2006). If we apply the method of obtaining bulk strain from lattice strain for elastic compression to plastic compression, the one-dimensional bulk strain will thus be underestimated. The strain deficit is compensated by the deformation along the other two directions. This method, intended for elastic compression, fails
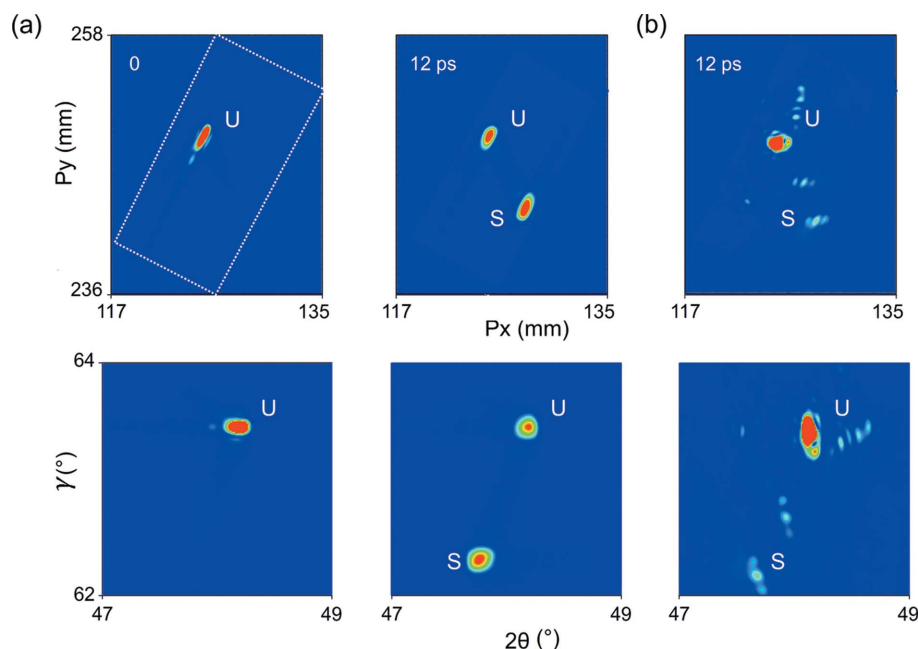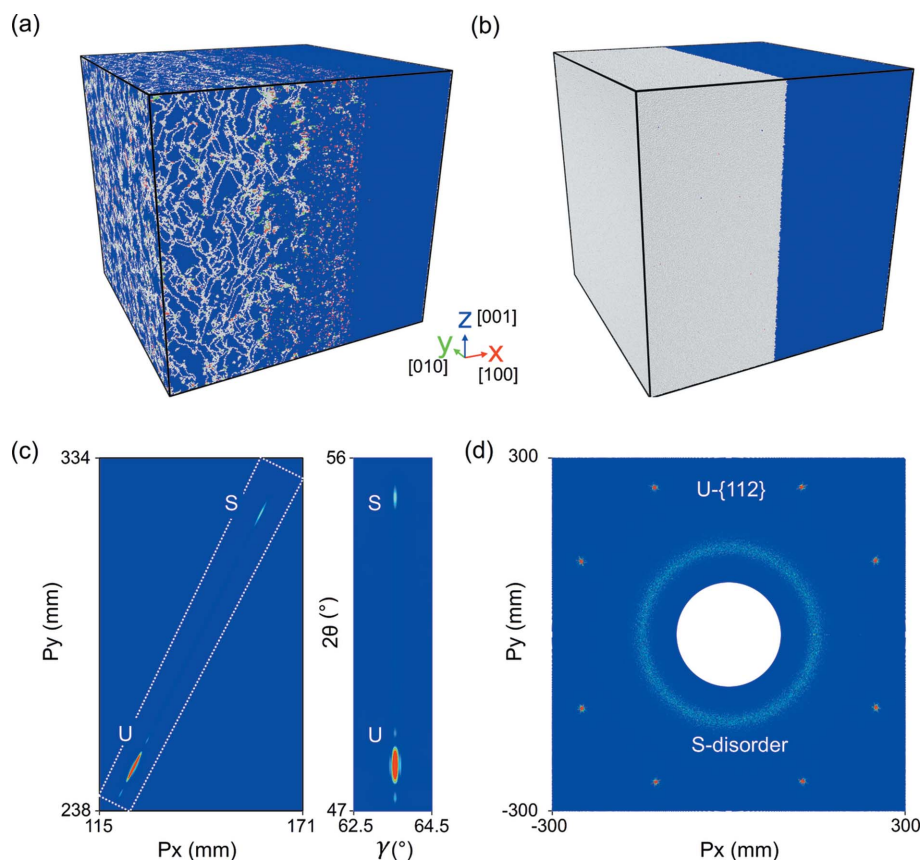

Figure 9
Snapshots of diffraction without (*a*) and with (*b*) edge release, for the ($\bar{1}12$) reflection. Top row: diffraction patterns; bottom row: γ–2θ maps corresponding to the area delimited by the dotted rectangle in the diffraction pattern. Color coding is based on scattering intensity. Shock direction: [100]; incident beam direction: [0$\bar{1}$0]; piston velocity: 0.2 km s^{-1}; $t = 0$ and 12 ps in (*a*); $t = 12$ ps in (*b*).

Figure 10
Snapshots of atomic configurations for (*a*) u_p = 0.75 km s^{-1} at 15 ps and (*b*) 2 km s^{-1} at 10 ps. (*c*) Diffraction pattern and 2θ–γ map for the $(\bar{1}12)$ reflection corresponding to (*a*). (*d*) Diffraction pattern corresponding to (*b*). Color coding is based on common neighbor analysis for (*a*) and (*b*) and scattering intensity for (*c*) and (*d*). Shock direction: [100]; incident beam direction: [100]; no edge release.

completely for the case of disordering induced by strong shocks (u_p = 2 km s^{-1}).

4. Conclusions

We perform large-scale molecular dynamics simulations of single-crystal tantalum under one-dimensional-strain shock compression, and simulate corresponding X-ray diffraction patterns to guide experimental design and data interpretation. Different shock loading conditions are explored, including purely elastic deformation, elastic–plastic two-wave structure and severe plastic deformation, and edge release. We obtain diffraction patterns and reciprocal space nodes from atomic configurations, and their interpretation is presented within the context of bulk and microscopic deformation and loading condition. For synchrotron diffraction experiments on single crystals under shock loading, a preferred geometry is the transmission mode (Laue geometry) to circumvent the edge release effect. The exact geometry should consider crystallographic orientation, loading direction, incident beam direction, X-ray spectrum bandwidth, and realistic detector size. To deduce bulk strain, the conventional *d*-spacing method is not appropriate, and a Laue geometry method is proposed

for the elastic deformation regime; however, caution should be exercised in the case of plastic deformation.

References

An, Q., Luo, S. N., Han, L. B., Zheng, L. Q. & Tschauner, O. (2008). *J. Phys. Condens. Matter*, **20**, 095220.

Bringa, E. M., Rosolankova, K., Rudd, R. E., Remington, B. A., Wark, J. S., Duchaineau, M., Kalantar, D. H., Hawreliak, J. & Belak, J. (2006). *Nat. Mater.* **5**, 805–809.

DeCamp, M. F., Reis, D. A., Fritz, D. M., Bucksbaum, P. H., Dufresne, E. M. & Clarke, R. (2005). *J. Synchrotron Rad.* **12**, 177–192.

E, J. C., Wang, L., Chen, S., Zhang, Y. Y. & Luo, S. N. (2018). *J. Synchrotron Rad.* **25**, 604–611.

Fan, D., Huang, J. W., Zeng, X. L., Li, Y. E. J. C., Huang, J. Y., Sun, T., Fezzaa, K., Wang, Z. & Luo, S. N. (2016). *Rev. Sci. Instrum.* **87**, 053903.

Gupta, Y. M., Turneaure, S. J., Perkins, K., Zimmerman, K., Arganbright, N., Shen, G. & Chow, P. (2012). *Rev. Sci. Instrum.* **83**, 123905.

Hahn, E. N., Germann, T. C., Ravelo, R., Hammerberg, J. E. & Meyers, M. A. (2017). *Acta Mater.* **126**, 313–328.

Holian, B. L. (1995). *Shock Waves*, **5**, 149–157.

Huang, J. Y., Huang, J. W., Sun, T., Fezzaa, K., Xu, S. L. & Luo, S. N. (2016). *Acta Mater.* **114**, 136–145.

Ichiyanagi, K., Adachi, S., Nozawa, S., Hironaka, Y., Nakamura, K. G., Sato, T., Tomita, A. & Koshihara, S. (2007). *Appl. Phys. Lett.* **91**, 231918.

Ichiyanagi, K. & Nakamura, K. G. (2016). *Metals*, **6**, 17.

Kalantar, D. H., Belak, J., Bringa, E., Budil, K., Caturla, M., Colvin, J., Kumar, M., Lorenz, K., Rudd, R., Stölken, J., Allen, A. M., Rosolankova, K., Wark, J. S., Meyers, M. A. & Schneider, M. (2003). *Phys. Plasmas*, **10**, 1569–1576.

Kraus, D., Ravasio, A., Gauthier, M., Gericke, D. O., Vorberger, J., Frydrych, S., Helfrich, J., Fletcher, L. B., Schaumann, G., Nagler, B., Barbrel, B., Bachmann, B., Gamboa, E. J., Göde, S., Granados, E., Gregori, G., Lee, H. J., Neumayer, P., Schumaker, W., Döppner, T., Falcone, R. W., Glenzer, S. H. & Roth, M. (2016). *Nat. Commun.* **7**, 10970.

Lane, J. M. D., Foiles, S. M., Lim, H. & Brown, J. L. (2016). *Phys. Rev. B*, **94**, 064301.

Liss, K.-D., d'Almeida, T., Kaiser, M., Hock, R., Magerl, A. & Eloy, J. F. (2009). *J. Appl. Phys.* **106**, 044914.

Lu, L., Bie, B. X., Li, Q. H., Sun, T., Fezzaa, K., Gong, X. L. & Luo, S. N. (2017a). *Acta Mater.* **132**, 389–394.

Lu, L., Huang, J. W., Fan, D., Bie, B. X., Sun, T., Fezzaa, K., Gong, X. L. & Luo, S. N. (2016). *Acta Mater.* **120**, 86–94.

Lu, L., Sun, T., Fezzaa, K., Gong, X. L. & Luo, S. N. (2017*b*). *Mater. Sci. Eng. A*, **701**, 143–148.

Luo, S. N., An, Q., Germann, T. C. & Han, L. B. (2009). *J. Appl. Phys.* **106**, 013502.

Luo, S. N., Jensen, B. J., Hooks, D. E., Fezzaa, K., Ramos, K. J., Yeager, J. D., Kwiatkowski, K. & Shimada, T. (2012). *Rev. Sci. Instrum.* **83**, 073903.

Plimpton, S. (1995). *J. Comput. Phys.* **117**, 1–19.

Prince, E. (2004). *International Table for Crystallography*, 3rd ed. Norwell: Kluwer Academic Publishers.

Ravelo, R., Germann, T. C., Guerrero, O., An, Q. & Holian, B. L. (2013). *Phys. Rev. B*, **88**, 134101.

Rigg, P. A. & Gupta, Y. M. (2001). *Phys. Rev. B*, **63**, 094112.

Sánchez del Río, M. & Dejus, R. J. (2004). *Proc. SPIE*, **5536**, 171–174.

Tang, M. X. E. J. C., Wang, L. & Luo, S. N. (2017). *J. Appl. Phys.* **121**, 115901.

Thierry d'Almeida, M., Kaiser, M., Di Michiel, T. & Buslaps, A. F. (2002). *Proc. SPIE*, **4780**, doi: 10.1117/12.469723.

Turneaure, S. J., Sharma, S. M., Volz, T. J., Winey, J. M. & Gupta, Y. M. (2017). *Sci. Adv.* **3**, eaao3561.

Wang, L. E. J. C., Cai, Y., Zhao, F., Fan, D. & Luo, S. N. (2015). *J. Appl. Phys.* **117**, 084301.

Wang, L., Zhao, F., Zhao, F. P., Cai, Y., An, Q. & Luo, S. N. (2014). *J. Appl. Phys.* **115**, 053528.

Warren, B. E. (1969). *X-ray Diffraction*. Courier Corporation.

Wehrenberg, C. E., McGonegle, D., Bolme, C., Higginbotham, A., Lazicki, A., Lee, H. J., Nagler, B., Park, H.-S., Remington, B. A., Rudd, R. E., Sliwa, M., Suggit, M., Swift, D., Tavella, F., Zepeda-Ruiz, L. & Wark, J. S. (2017). *Nature (London)*, **550**, 496–499.

Williams, D. B. & Carter, C. B. (2009). *Transmission Electron Microscopy*, Part. 2, *Diffraction*. Springer.